Topology-Optimized 2D Silicon-Air Phononic Crystal Slabs for Enhancing Quality Factor of Laterally Vibrating Resonators

Zihao Xie[a], Yongqing Fu[b], Jin Xie[a,*]

[a] *State Key Laboratory of Fluid Power and Mechatronic Systems, Zhejiang University, Hangzhou 310027, China*

[b] *Faculty of Engineering and Environment, University of Northumbria, Newcastle upon Tyne NE1 8ST, UK*

*Corresponding author. E-mail address: xiejin@zju.edu.cn (Jin Xie)

Abstract: 2D Phononic crystal (PnC) slabs have shown advantage in enhancing the quality factors (*Q*) of piezoelectric laterally vibrating resonators (LVRs) through topology optimization. However, the narrow geometries of most topology-optimized silicon-air 2D PnC slabs are facing significant fabrication challenges owing to restricted etching precision, and anisotropic nature of silicon is frequently overlooked. To address these issues, this study employs finite element analysis (FEA) with appropriate discretization numbers and genetic algorithm (GA) to optimize the structures and geometries of 2D silicon-air PnC slabs. The optimized square lattice PnC slabs, featured with a rounded-cross structure oriented along the <110> directions of silicon, achieve an impressive relative bandgap (RBG) width of 82.2% for in-plane modes. When further tilted by 15 degrees from the <100> directions within the (001) plane, the optimal RBG width is expanded to 91.4%. We fabricated and characterized thin-film piezoelectric-on-silicon LVRs, with or without optimized 2D PnC slabs. The presence of PnC slabs around anchors increases the series and parallel quality factors (i.e., Q_s and Q_p) from 2240 (and 2237) to 7118 (and 7501) respectively, with the PnC slabs oriented along the <110> directions of silicon.

Keywords: Laterally vibrating resonators, Phononic crystal slabs, Topology optimization, Quality factor

Article Highlights

- Finite element analysis with genetic algorithm is utilized to optimize the structures and geometries of 2D silicon-air phononic crystal slabs.
- The optimal relative bandgap of optimized silicon-air phononic crystal slabs is 91.4%.
- Fabricated laterally vibrating resonators show increased quality factor from 2237 to 7501.

1. Introduction

Piezoelectric resonators are crucial in radio frequency (RF) communication due to their compact size, cost-effectiveness, high performance, and compatibility with complementary metal-oxide-semiconductor (CMOS) process. Two of commonly used types are surface acoustic wave (SAW) resonators and thin film bulk acoustic wave resonators (FBARs).[1] SAW resonators, known for their easy fabrication and consistent performance, facing challenges in the super-high-frequency (SHF) range due to the limited phase velocity.[2] FBARs have an ultrahigh working frequency and miniature dimensions; however, integrating multiple frequencies onto a single FBAR chip is complex due to its operational thickness-extensional mode. To circumvent these limitations, laterally vibrating resonators (LVRs) operating in the lowest symmetrical (S_0) mode have emerged.[3,4] These LVRs feature a high phase velocity and a resonant frequency primarily determined by in-plane dimensions, which can be tuned through lithography, and exhibit minimal phase velocity dispersion.[5]

A high quality factor (*Q*) of LVRs is essential for low-phase-noise oscillators[6] and low insertion loss filters.[7] Various approaches have been proposed to enhance the *Q* value by investigating intrinsic and extrinsic loss mechanisms, with anchor loss (Q_{anc}) being identified as a significant contributor to extrinsic losses for bulk mode resonators.[1,8-10] Numerous strategies have been suggested to increase Q_{anc}, such as frame geometry optimizations, etching notches, and reflector structures

around tethers.[1,9,10] Thin-film piezoelectric-on-silicon (TPoS) LVRs have also been extensively studied for their higher Q values owing to the high intrinsic Q value of single-crystal silicon.[11,12] Recently, two-dimensional phononic crystal (2D PnC) slabs have been employed in LVRs to enhance the Q_{anc} by reducing the elastic wave leakage from resonator anchors, demonstrating a higher Q value compared to other methods.[8,13-16]

Lee et al. recently employed PnC slabs to increase the Q factor of piezoelectric LVRs, yielding a notable enhancement factor up to 4.2.[13,15,17] Similarly, utilization of PnC tethers in electrostatic width-extensional resonators led to a maximal Q enhancement factor of 2.4.[14] Moreover, for low-frequency flexural resonators, application of PnC strip in a silicon cantilever resonator at a frequency of 2 MHz resulted in a remarkable Q enhancement factor of 27.[18] Compared with the cantilever resonator, other loss mechanisms such as interfacial dissipation and thermal elastic damping of electrodes limit the Q factor enhancement of piezoelectric LVRs.[19,20]

Traditional unit cell structures such as air-holes[13] and cross-inclusions[21-23] with one- or two-dimensional periodicity have been utilized in various resonators, but the maximum achievable relative bandgap (RBG) width of PnC slabs using these experience-selected unit cell structures is limited. Topology optimization can be utilized to maximize the RBG by systematically altering the unit cell structure.[24] The use of computational tools such as genetic algorithm (GA) in this optimization process not only expedites the design cycle but also uncovers novel structures that otherwise might be unintuitive.[25,26] However, the optimized structures often exhibit narrow geometries[27,28], are difficult to fabricate with limited etching precision (minimal feature size of 2 μm, typically), particularly for the precisely tuning the optimization procedures[29] and the differences in crystal orientations of silicon are often neglected when arranging the PnC slab.[13,28,30]

To solve this issue, in this paper, we use FEM and GA methods to perform topology optimization of 2D silicon-air PnC slabs that are easily manufacturable, considering the anisotropy of silicon. The optimal rounded-cross PnC slab achieves a maximal RBG of 82.2% for in-plane modes along the <110> directions of silicon, and of 91.4% when arranged 15 degrees to <100>. The fabricated aluminum nitride (AlN) TPoS LVRs show significantly enhanced series and parallel quality factors (i.e., Q_s and Q_p) when the rounded-cross PnC slabs are positioned around anchors along the <110> directions.

2. FEM Modeling of 2D PnC Slabs

Elastic wave propagation in 2D PnC slabs can be accurately described by the Bloch's theorem.[31] Specifically, the 2D displacement field $\boldsymbol{u}(\boldsymbol{r})$ can be represented as a modulated plane wave,

$$\boldsymbol{u}(\boldsymbol{k},\boldsymbol{r}) = \boldsymbol{u}_{\boldsymbol{k}}(\boldsymbol{r})\exp(-j\boldsymbol{k}\cdot\boldsymbol{r}) \quad (1)$$

where $\boldsymbol{u}_{\boldsymbol{k}}(\boldsymbol{r})$ has the same spatial periodicity as the lattice, with $\boldsymbol{k} = (k_x, k_y)$ and $\boldsymbol{r} = (x, y)$ representing the Bloch wave vector and position vector, respectively.

Considering a square lattice composed of silicon and air holes shown in Fig. 1(a), FEM can be utilized to determine the band structures of the 2D PnC slab, with the unit cell discretized into $N \times N$ square elements, as shown in Fig. 1(b). The equations of motion governing the in-plane displacement $\boldsymbol{u} = [u, v]^T$ in the x-y plane for anisotropic silicon under plane stress assumption are given by[32,33]

$$\rho\omega^2 u_i = \boldsymbol{L}_{im}\boldsymbol{C}_{mn}\boldsymbol{L}_{nj}^T u_j \quad (2)$$

The elastic strain operator matrix $\boldsymbol{L}$ and the stiffness matrix $\boldsymbol{C}$ are given as:

$$\boldsymbol{L} = \begin{bmatrix} \partial/\partial x & 0 & \partial/\partial y \\ 0 & \partial/\partial y & \partial/\partial x \end{bmatrix}, \boldsymbol{C} = \begin{bmatrix} \tilde{c}_{11} & \tilde{c}_{12} & 0 \\ \tilde{c}_{12} & \tilde{c}_{11} & 0 \\ 0 & 0 & \tilde{c}_{44} \end{bmatrix} \quad (3)$$

and

$$\begin{cases} \tilde{c}_{11} = c_{11}^{'} - \dfrac{c_{12}^{'2}}{c_{11}} \\ \tilde{c}_{12} = c_{12}^{'} - \dfrac{c_{12}^{'2}}{c_{11}} \end{cases} \begin{cases} c_{11}^{'} = c_{11} - \dfrac{c_{11} - c_{12} - 2c_{44}}{2} \sin^2 2\theta \\ c_{12}^{'} = c_{12} + \dfrac{c_{11} - c_{12} - 2c_{44}}{2} \sin^2 2\theta \end{cases} \tag{4}$$

where $c_{11} = 166$ MPa, $c_{12} = 64$ MPa, and $c_{44} = 80$ MPa are the elastic constants of silicon along the <100> orientation. ω is the angular frequency of the time-dependent harmonic term $\exp(-j\omega t)$. The *z*-axis of the global coordinate system is aligned with the [001] silicon crystal direction, while the *x*- and *y*- axes are rotated from the [100] and [010] silicon crystal directions with an angle θ, as depicted in Fig. 1(b).

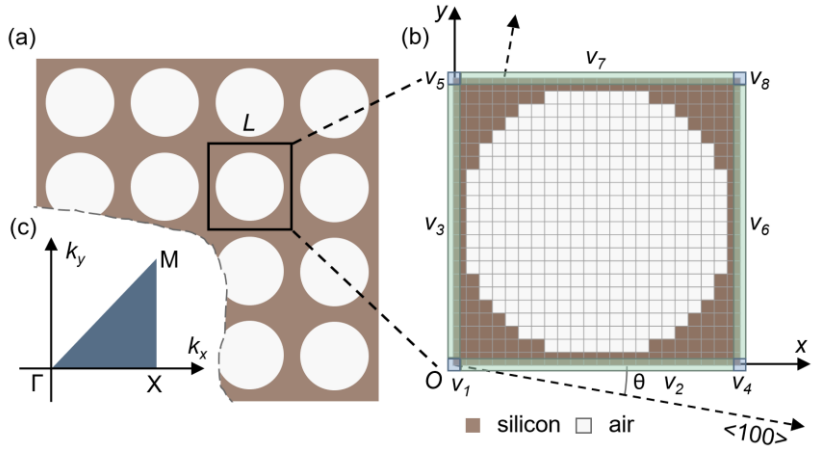

Fig.1 (a) Schematic diagram of the 2D PnC slab, with L denoting the lattice pitch; (b) the discrete unit cell of silicon-air PnC slabs and displacements of boundary nodes $\boldsymbol{v}_i, i = 1 \ldots 8$; (c) the irreducible BZ of the square lattice in the reciprocal space, with $\Gamma(0,0)$, $X(\pi/L, 0)$, and $M(\pi/L, \pi/L)$.

The band structure calculation of silicon-air PnC slabs is mainly focused on the in-plane modes due to the dominance of transverse displacements in the resonant mode of LVRs. Simultaneously, leaked waves exhibit substantial in-plane vibrations.[3] Furthermore, for PnC slabs with common thickness-to-unit cell length ratios, such as 0.5, the in-plane modes calculated using the plane stress assumption are very close to the results obtained through the three-dimensional constitutive equation.[13,30] Consequently, the plane stress assumption is adopted to simplify the calculations.

When Eq. (2) is numerically solved with the FEM, the eigenvalue equation is discretized as[31]

$$\boldsymbol{v}^T(\boldsymbol{K} - \omega^2 \boldsymbol{M})\boldsymbol{v} = 0 \tag{5}$$

where $\boldsymbol{v}$ is a vector representing displacements of all element nodes of silicon. Air elements are generally excluded from the calculation of elastic waves due to the significantly lower acoustic impedance of air in comparison to those of solid materials. The free boundary conditions are then enforced at the interface of the air-hole. $\boldsymbol{K}$ and $\boldsymbol{M}$ are the global stiffness and mass matrices of the unit cell, respectively. The periodicity results in periodic boundary conditions in both *x*- and *y*-directions. These conditions are related to the displacements of the four edges of the unit cell as $\boldsymbol{u}(x = L) = \boldsymbol{u}(x = 0)\exp(-jk_x L)$ and $\boldsymbol{u}(y = L) = \boldsymbol{u}(y = 0)\exp(-jk_y L)$. Thus, the degrees of freedom (DOFs) of the boundary nodes are independent. Linear transformation matrix $\mathbf{\Gamma}(\boldsymbol{k})$ can be used to eliminate redundant DOFs, representing $\boldsymbol{v}$ without $\boldsymbol{v}_i, \mathrm{i} = 4, \cdots, 8$. Substituting the transform relation yields the dispersion relation:

$$|\boldsymbol{D}(\omega, \boldsymbol{k})| = |\boldsymbol{\Gamma}^T(\boldsymbol{k})\boldsymbol{K}\boldsymbol{\Gamma}(\boldsymbol{k}) - \omega^2 \boldsymbol{\Gamma}^T(\boldsymbol{k})\boldsymbol{M}\boldsymbol{\Gamma}(\boldsymbol{k})| = 0 \tag{6}$$

Furthermore, eigenfrequencies of the PnC slabs exhibit a periodicity in reciprocal space ($\boldsymbol{k}$-space) and share the same point group symmetry as the lattice in the real space. The irreducible Brillouin zone (BZ) encompasses all possible eigenvalues $\omega(\boldsymbol{k})$ and eigenmodes $\boldsymbol{u}(\boldsymbol{k}, \boldsymbol{r})$, reaching extreme values when the wave vector is along with the boundary of the irreducible BZ. To calculate band structures of the PnC slabs, only the Bloch wave vectors on the boundary of the irreducible BZ

are considered. For the square unit cell, the irreducible BZ in reciprocal space is illustrated in Fig. 1(c), including points $\Gamma(0,0)$, $\mathrm{X}(\pi/L, 0)$, and $\mathrm{M}(\pi/L, \pi/L)$, forming a triangular boundary.

3. Topology Optimization of 2D PnC Slabs

After obtaining the band structure of 2D PnC slabs, the RBG between the adjacent bands can be calculated as

$$\mathrm{RBG} = \frac{\Delta\omega_n}{\omega_n^c} = 2\frac{\min_{\boldsymbol{k}}\omega_{n+1}(\boldsymbol{k}) - \max_{\boldsymbol{k}}\omega_n(\boldsymbol{k})}{\min_{\boldsymbol{k}}\omega_{n+1}(\boldsymbol{k}) + \max_{\boldsymbol{k}}\omega_n(\boldsymbol{k})} \tag{7}$$

where $\Delta\omega_n$ and ω_n^c represent the bandgap width between the n-th and $(n+1)$-th bands and the middle frequency of the corresponding bandgap, respectively. Notably, the RBG exists only when $\Delta\omega_n > 0$.

The GA procedure for topology optimization of the RBG of a square-lattice 2D silicon-air PnC slab can be described as follows:

(i) Each discrete element (referred to as 'gene' in the GA terminology) in the unit cell can either be silicon or air with a binary variable of 1 or 0. The topology of the unit cell (referred to as 'chromosome' in the GA terminology) can be represented with the matrix $\boldsymbol{X} = [x_{ij}]_{N\times N}$. Initially, N_p (e.g., 12 in the present work) chromosomes are created and the N^2 genes in each chromosome are randomly assigned to 1 or 0 while maintaining the symmetry of the square unit cell. Typically, chromosomes with randomly selected genes have no bandgap. To expedite the iteration process, some chromosome seeds are often provided at the beginning, and the iteration continues based on the seeds;

(ii) After the first generation of chromosomes are created, the RBG (referred to as 'fitness' in GA terminology) between the n-th and $(n+1)$-th bands of the chromosomes are calculated using the FEM. The fitness is set to a small value (e.g., 0.001 in the present work) if the chromosome has no bandgap;

(iii) Create the next generation of N_p chromosomes:

a. The N_p parent chromosomes are generated firstly: The chromosomes of the previous generation are sorted by fitness from lower to higher. Then a random number is generated ranging from 0 to 1, and the k-th chromosome is selected if the random number falls into the interval $[p_{k-1}, p_k]$, where

$$p_k = p_{k-1} + \frac{2(N_p - k + 1)}{N_p(N_p + 1)}, k = 1, \ldots, N_p \tag{8}$$

and $p_0 = 0$;

b. The next step is crossover: Randomly pair the N_p parent chromosomes first. For each pair, the parents are crossed over with a probability P_c (e.g., 0.9 in the present work), i.e., randomly exchange the genes of parent chromosome to produce two chromosomes for the new generation;

c. Nest is mutation step: Each gene of the new generation chromosomes is muted with a probability P_m (e.g., 0.02 in the present work), i.e., change x_{ij} into $1 - x_{ij}$;

d. For each pair in (b), if the better fitness value of the two offspring chromosomes after mutation is less than that of their parent chromosomes, the offspring chromosomes are replaced by their parent chromosomes;

(iv) The step (iii) is repeated until the maximum allowable number of iterations (800 in the present work) is reached.

Porous phononic crystal slabs appear to possess enhanced RBG.[34] However, the optimization algorithms for these structures tend to highly complicated and minimize the width of connecting

components among distinct solid parts. This erosion is aimed at enhancing the RBG by reducing the rigidity of these connecting components. Nevertheless, the outcomes of this structural approach greatly rely on the width of the connecting components, making them sensitive to the mesh.[24,30] To address this challenge, a simple solution is proposed by designating the boundary elements as unalterable silicon. By starting the iteration from a single-hole unit-cell, this approach can limit excessive reduction in the overall structure's rigidity, thereby mitigating its dependence on the mesh. Furthermore, meshing structures may contain isolated silicon components, which can be excluded when three zero eigenvalues are present due to the lack of boundary constraints.

Topology optimization of 2D PnC slabs with FEM relies on the discrete number N, significantly impacting the optimal structure. Higher N values improve shape resolution and yield more accurate RBG results, but may create excessively narrow geometries unsuitable for microfabrication owing to the limited etching resolution. While the relatively coarse mesh in FEM can cause errors, it offers insight into optimal structures. A compromise value of $\mathrm{N} = 22$ is chosen in this study, with other parameters as $N_p = 12$, $P_c = 0.9$, and $P_m = 0.02$. The choice of n plays a crucial role in determining the optimal unit cell shape and corresponding optimal RBG, with the RBG between the third and fourth bands is optimized initially, assuming that the PnC slabs are arranged along the <110> directions ($\mathrm{n} = 3, \theta = 45°$). The FEM calculations with linear 4-node square elements, as well as the GA procedure, are implemented in Mathematica 13.1. Fig. 2 displays the best fitness of PnC slabs with the iteration of chromosome generations, and two different chromosome seeds (i.e., air-hole and cross-inclusion seed ones) are chosen. The silicon in the air-hole seed gradually shrinks towards the unit cell center, converging after 81 generations with an enhanced RBG from 33.0% to 92.8% for the optimal structure. Similarly, air holes in the cross-inclusion seed expand towards the boundary, converging more slowly than the air-hole seed but reaching the same structure after 219 generations.

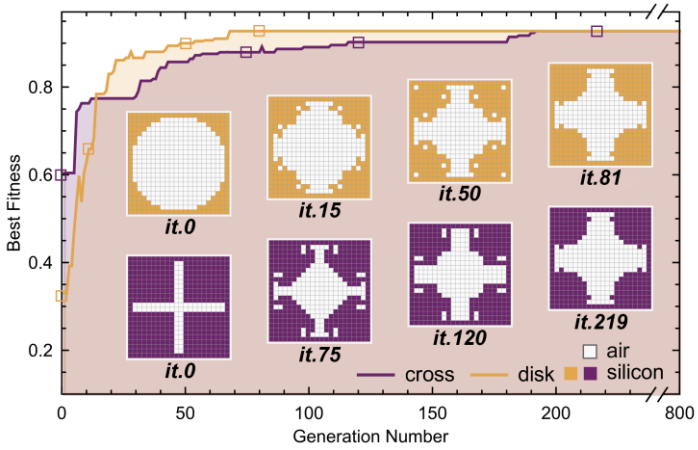

Fig.2 The best fitness of the square lattice 2D PnC slabs as the chromosome generations iterate. The seed chromosomes are air-hole (yellow) and cross-inclusion (purple).

The optimal unit cell shape for silicon-air PnC slabs is a rounded-cross with four rounded silicon corners and crossed air holes, characterized by parameters L, w_1, w_2, and r, as depicted in the inset of Fig. 3(c). L is set to 22 μm to ensure a suitable resonant frequency of LVR, while the other parameters are optimized. Starting with the assumption that rounded corners are neglected ($\mathrm{r} = 0$), RBG is calculated with different w_1 and w_2 dimensions and the obtained results are shown in Fig. 3(a). The band structures during the optimization procedure are calculated using COMSOL Multiphysics 5.6 for more precise results. Minimum line width is limited to 2 μm due to fabrication constraints, leading to a minimum w_1 of 1 μm. RBG is increased as w_1 decreases, so w_1 is fixed at 1 μm and further optimization involves w_2 and r. The chosen $w_1 = 1$ μm corresponds to the size of a single element, and a larger discrete number N can result in narrower boundary dimension w_1 and higher RBG values. However, the narrow structures are impractical for its fabrication. The maximal RBG of 82.0% for the rounded-cross PnC slab is achieved with w_2 at 6 μm and r at 5.5

μm as shown in Fig. 3(b). In contrast to the parameter w_1, the RBG is less sensitive to w_2 and r.

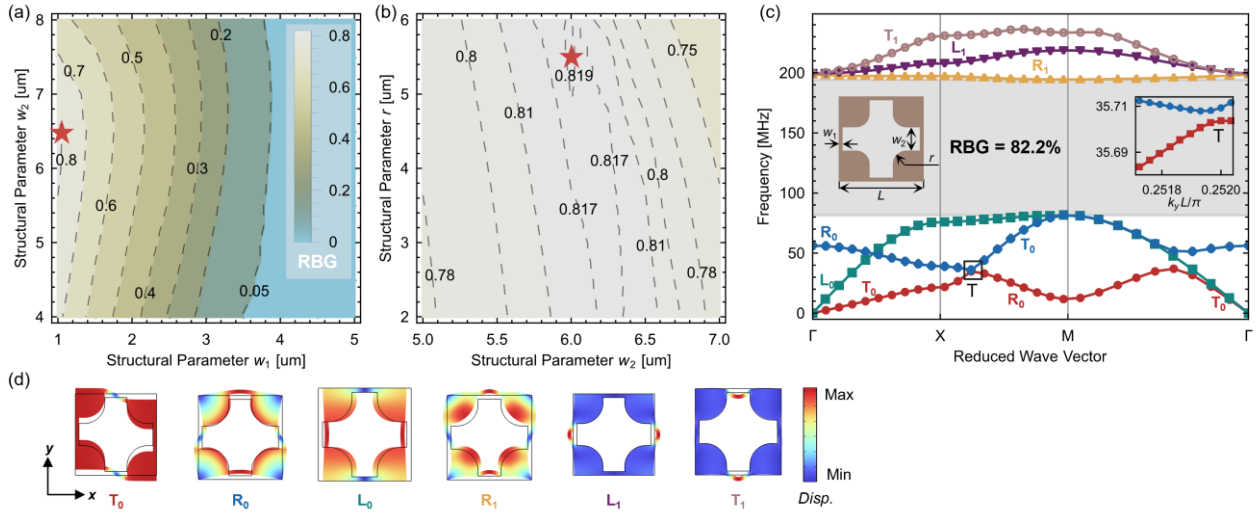

Fig.3 (a) RBG of rounded-cross PnC slabs with different w_1 and w_2, where $r = 0$ and $L = 22$ μm; (b) RBG of rounded-cross PnC slabs with different w_2 and r, where $w_1 = 1$ μm and $L = 22$ μm; (c) the band structure of the optimal rounded-cross PnC slab when $w_1 = 1$ μm, $w_2 = 6$ μm and $r = 5.5$ μm, with a bandgap ranging from 81 MHz to 194 MHz and the corresponding RBG of 82.2%. Both a unit cell of the rounded-cross PnC slab and the magnified view around the point T are shown in the inset; (d) displacement field diagrams of the lowest six in-plane modes for $\boldsymbol{k} = (\pi/L, 0)$.

As shown in Fig. 3(c), the band structure of the optimal rounded-cross PnC slab reveals an in-plane mode bandgap from 81 MHz to 194 MHz with an RBG of 82.2%. The lowest three dispersion branches are corresponding to the fundamental transverse (T_0), longitudinal (L_0), and rotational (R_0) modes.[35] For in-plane modes propagating along the x- direction (Γ-X), T_0 and L_0 modes exhibit dominant displacements along the y- and x- axes, respectively. Displacement field diagrams of the lowest six in-plane modes are shown in Fig. 3(d) for $\boldsymbol{k} = (\pi/L, 0)$. T_0 mode couples with R_0 mode[35,36], causing the two branches to bend away from each other and preventing crossover around point T[33], as observed in the magnified view in Fig. 3(c). Therefore, T_0 and R_0 modes exhibit rapid mode transitions around point T and gradual interconversion along the M- Γ section. The upper three branches are corresponding to the first transverse (T_1), longitudinal (L_1), and rotational (R_1) modes.

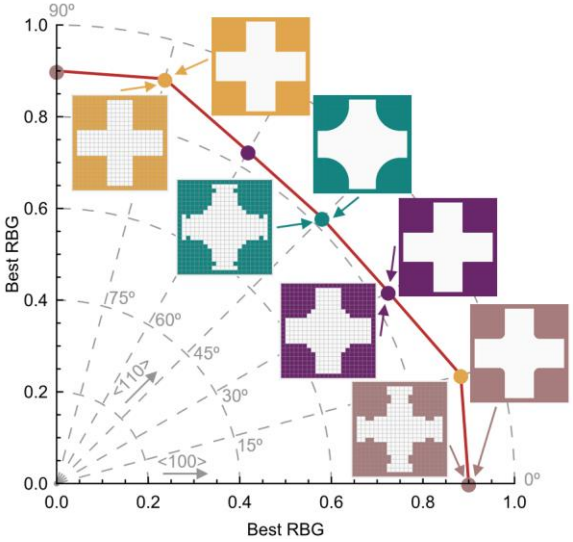

Fig.4 The optimal structures of the unit cell obtained through topology optimization and the optimal rounded-cross PnC slabs along different directions in the (001) plane of silicon.

The alignment of the PnC slab in the (001) plane of silicon affects both the band structure and the

optimal lattice geometry. Fig. 4 shows the optimal shapes for the bandgap between the third and fourth bands with various rotation angles θ ($0°$, $15°$, $30°$, and $45°$) in an all rounded-cross structures. Values of w_1, w_2, and r are then optimized for different directions, resulting in a maximum RBG of 91.4% when $\theta = 15°$.

The coupling between R_0 and T_0 modes and the finite phase velocity of L_0 and T_0 modes at the point Γ make it difficult to separate the three lower bands and obtain a bandgap. Therefore, topology optimization is also performed for the bandgap between the fourth and fifth bands, with an optimal RBG of 56%. This value is smaller than the optimal RBG observed when $n = 3$.

4. LVRs with Topology-Optimized Rounded-cross PnC slabs

The optimized rounded-cross PnC slabs oriented along the <110> directions are chosen as an example to investigate their bandgap properties. As silicon exhibits a lower Poisson's ratio along the <110> directions, reducing the energy leaked from LVR anchors.[37] The 2D PnCs are fabricated by etching holes into the device layer of silicon-on-insulator (SOI) substrate, limiting the thickness t of rounded-cross PnC to 10 μm.[38] Thickness dependence of in-plane bandgaps is illustrated in Fig. 5(a), wherein the normalized thickness t/L is considered. As the normalized thickness increases, specifically reaching 0.6, thickness-shear modes exhibit the decreased frequencies than those of the R_1 modes. The frequencies of thickness-shear modes continuously decrease with further increase of thickness. Consequently, the RBG experiences a reduction, leading to the eventual disappearance of the bandgap at a normalized thickness of 1.54. Furthermore, for the fabrication dimensions $t = 10$ μm and $L = 22$ μm, the normalized thickness falls within the plateau region of RBG. Band structures for both in-plane and out-of-plane modes of the rounded-cross PnC slab with thickness of 10 μm are illustrated in Fig. 5(b). In-plane modes exhibit a bandgap between L_0 and R_1 modes, ranging from 79 MHz to 195 MHz, with an RBG of 84.7%, slightly exceeding the result from 2D analysis. Numerous out-of-plane modes populate the bandgap of in-plane modes. Two complete bandgaps emerge within the frequency ranges of 95-143 MHz and 146-176 MHz, preventing all types of waves from propagating in any direction.

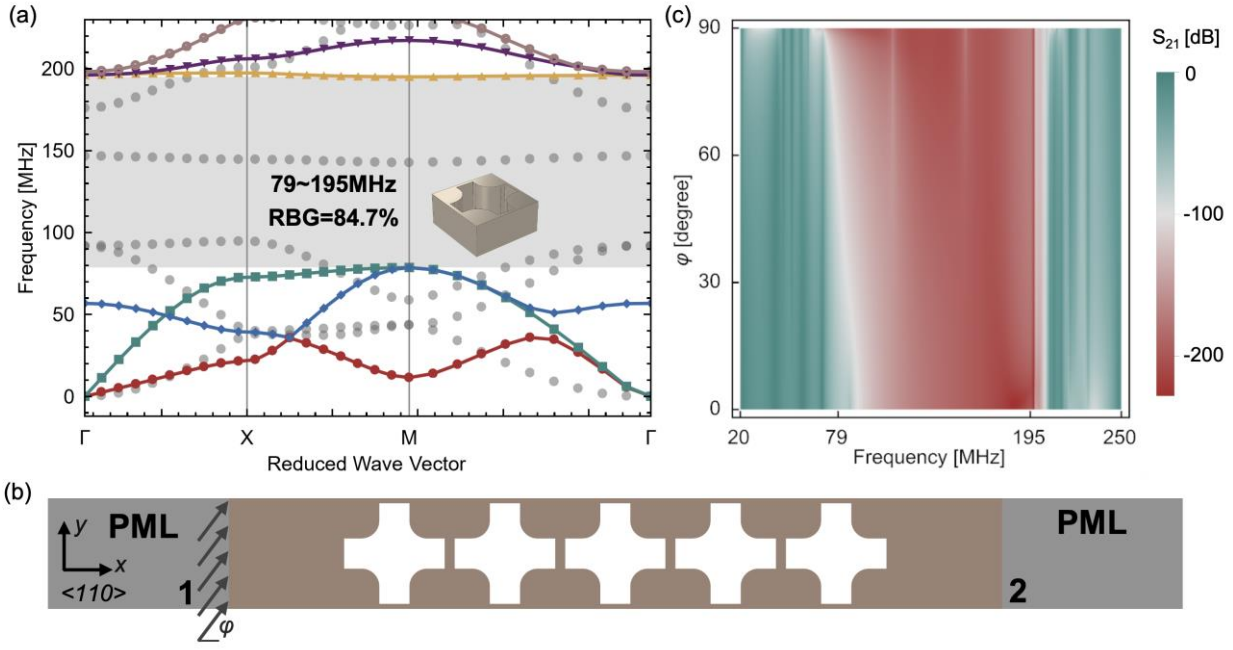

Fig.5 (a) Thickness dependence of in-plane bandgaps for optimized rounded-cross PnC slabs, dotted line denotes $t = 10$ μm and $L = 22$ μm for fabrication; (b) band structure of the 10 μm-thick optimized rounded-cross PnC slabs, with in-plane modes as colored lines and out-of-plane modes as gray dots. RBG of in-plane modes is 84.7%; (c) top view of the two-port system designed to evaluate the transmission of in-plane waves, featuring inner PnC slabs and outer PMLs; (d)

simulated S_{21} for ϕ from 0 to 90 degrees..

To validate the suppression efficiency of PnC slabs in suppressing in-plane waves within the in-plane bandgap, a two-port system with five columns of PnCs and outer perfectly matching layers (PMLs) is designed, as depicted in Fig. 5(c). The in-plane wave attenuation efficiency is characterized by the transmission signal S_{21}, defined as the ratio of power flow density integrals on both ports when the two ports are impedance matched[22]:

$$S_{21} = \frac{\int_{\Omega_2} \boldsymbol{P}_2 \cdot \boldsymbol{n}\, \mathrm{d}S}{\int_{\Omega_1} \boldsymbol{P}_1 \cdot \boldsymbol{n}\, \mathrm{d}S} = \frac{\int_{\Omega_2} -\frac{1}{2}\boldsymbol{v}_2^* \boldsymbol{T}_2 \cdot \boldsymbol{n}\, \mathrm{d}S}{\int_{\Omega_1} -\frac{1}{2}\boldsymbol{v}_1^* \boldsymbol{T}_1 \cdot \boldsymbol{n}\, \mathrm{d}S} \tag{9}$$

where $\boldsymbol{P}_1$, Ω_1 and $\boldsymbol{P}_2$, Ω_2 represent the incident (or transmitted) complex acoustic Poynting vector and the integral surface of ports 1 and 2, respectively. $\boldsymbol{v}_1(\boldsymbol{v}_2)$ and $\boldsymbol{T}_1(\boldsymbol{T}_2)$ represent the velocity and stress tensors of the corresponding ports, respectively, while $\boldsymbol{n}$ denotes the normal of the two surfaces. Here $-1/2$ and the conjugate transpose (*) account for time harmonic fields. Periodic boundary conditions are implemented to the *y*-edges of the system, while boundary loads with angle φ relative to the *x*-axis are applied on port 1. Low-reflective boundary conditions are set to the *x*-edges of two ports to eliminate the reflection. The simulated S_{21} values for angles φ from 0 to 90 degrees are displayed in Fig. 5(d). The S_{21} undergoes a significant attenuation, reaching -200 dB within the bandgap for the in-plane modes across all directions.

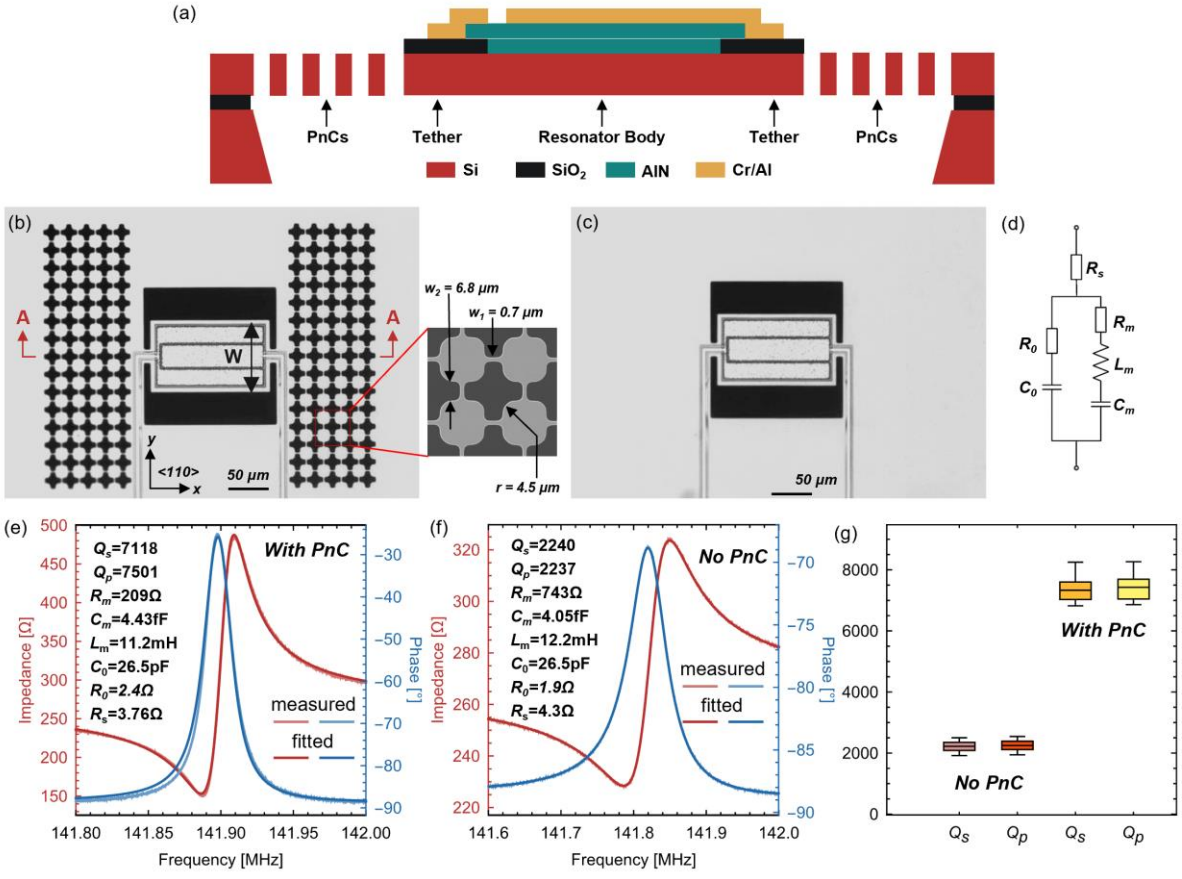

Fig.6 (a) Cross-section view schematic taken along line A-A; optical micrograph of the fabricated TPoS LVRs (b) with five columns of PnC slabs around each anchor and (c) without PnC slabs; zoom-in view of fabricated PnC slab are also shown in the inset; (d) schematic diagram of MBVD model; (e) the measured and fitted impedances of the LVR with PnC slabs around the anchors; (f) the measured and fitted impedances of the LVR without PnC slabs around the anchors; (g) extracted values of Q_s and Q_p for LVRs with and without PnC slabs.

Utilizing the in-plane wave suppression capabilities of the rounded-cross PnC slabs, energy leakage from LVR anchors can be reduced by positioning the PnC arrays around the anchors. PnC slabs can reflect vertical elastic waves leaking from anchors and store more elastic energy in the

resonator body.[13,22] Some free spaces between anchors and PnC arrays are utilized for electrical connection. To further suppress the propagation of the in-plane waves, the resonant frequency of LVR is placed around the center of bandgap of in-plane modes. The resonator operates in the lowest quasi-symmetric (QS_0) mode, with its resonant frequency determined by the phase velocity (v) and wavelength (λ) as:

$$f_r = \frac{v}{\lambda} \tag{10}$$

The lateral dimension of LVR corresponds to an integer multiple of half the wavelength, $W = n \times \lambda/2$, where n represents the order of the QS_0 mode.

The TPoS LVRs were fabricated using the commercial PiezoMUMPs process[38], as illustrated in Fig. 6(a). The LVR bodies and PnC slabs were formed by depositing and patterning a 0.5 µm-thick *c*-oriented AlN piezoelectric film and 1.02 µm-thick Cr/Al electrodes, followed by etching the device layer of SOI. Subsequently, the bottom silicon and buried oxide layers were removed using by reactive ion etching (DRIE) and wet etching. The fabricated LVRs, featuring five rows of the optimized rounded-cross PnC slabs surrounding each anchor, and those without PnC slabs, are shown in Figs. 6(b) and 6(c). These LVRs are operated in the third QS_0 mode with $W = 90$ µm and a resonant frequency of 142 MHz, based on the three-dimensional simulation results. The zoomed-in SEM image of the single unit cell of PnC slabs in the inset of Fig. 6(b) and measured the detailed structural parameters: $w_1 = 0.7$ µm, $w_2 = 6.7$ µm, and $r = 4.5$ µm. The simulated bandgap of fabricated PnC slab is 67-166 MHz, compared to the optimized bandgap of 79-195 MHz. The RBG increased slightly from 84.7% to 84.9%, which is a negligible error. However, the center of the bandgap decreased from 137 MHz to 117 MHz, moving away from the resonant frequency at 141 MHz. This shift may result in a lower *Q* factor than initially expected.

Electrical characterizations were then performed on both LVRs using a network analyzer. Impedances were extracted from the one-port resonators by measuring the S_{11} parameter. The measured magnitude and phase of impedance for both LVRs are depicted in Figs. 6(d), 6(e), and 6(f). Series resonant frequencies are 141.78 MHz and 114.89 MHz for the LVRs with and without the PnC slabs, respectively. The measured impedance data were fitted using the Modified-Butterworth-Van Dyke (MBVD) model[39] with the least squares method, as illustrated in Figs. 6(e) and 6(f). The LVR without PnCs exhibited Q_s and Q_p values of 2240 and 2237, respectively, along with R_m of 743 Ω and motional capacitance (C_m) of 4.05 fF. In contrast, the LVR with PnC slabs displayed the significantly increased Q_s and Q_p values of 7118 and 7501, a decreased R_m of 209 Ω, and a C_m of 4.43 fF. Five samples of each of the two resonator types are further tested (i.e., a total of 10 samples tested) to evaluate repeatability. The extracted values of Q_s and Q_p for LVRs with and without PnC slabs are shown in Fig. 6(g). The mean values for TPoS LVRs with PnC slabs are Q_s = 2213 and Q_p = 2238. For TPoS LVRs without PnC slabs, the mean values are Q_s = 7317 and Q_p = 7414. These results demonstrated the effectiveness of the PnC slabs around the anchors in reducing anchor loss of LVRs, thereby improving Q_s (Q_p) and reducing R_m. Compared to previous designs, LVRs with rounded-cross PnCs exhibit higher *Q* values, especially when larger electrode duty factors are employed, indicating increased ohmic and thermoelastic losses.[17]

5. Conclusion

Using FEM and GA, we developed a rounded-cross unit cell that maximizes RBG and is suitable for fabrication, addressing narrow geometries in topology optimized silicon-air PnC slabs, while also considering the anisotropy. The optimal PnC slabs exhibit a maximal RBG of 82.2% for in-plane modes along <110> directions, and 91.4% at a deviation of 15 degrees from <100> directions within the (001) plane. Incorporating these designs along the <110> directions into TPoS LVRs significantly boosts the Q_s (Q_p) from 2240 (2237) to 7118 (7501). This work highlights the potential of topology optimization for designing easily fabricated PnC slab structures that account for material

anisotropy, enabling high-performance resonators. The optimized silicon-air PnC slabs can also benefit other silicon-based applications for wave guiding and focusing.[40,41]

Acknowledgments

This work is supported by the Zhejiang Provincial Natural Science Foundation of China (LZ24E050002) and the National Natural Science Foundation of China (Grant 52175552).

Conflict of interest

The authors have no conflicts to disclose.

Data availability

The data that support the findings of this study are available from the corresponding authors upon reasonable request.

References

Reference to a journal publication:
1. Z. Luo, S. Shao, K. Liu, Y. Lu, A. Mazzalai, C. Tosi, and T. Wu. Al0.7Sc0. 3N butterfly-shaped laterally vibrating resonator with a figure-of-merit (kt2·Qm) over 146. Appl. Phys. Lett. 2022;120:173508. https://doi.org/10.1063/5.0090226
2. J. Zou, C. Lin, C. Lam, and A. Pisano. Transducer design for AlN Lamb wave resonators. J. Appl. Phys. 2017;121:154502. https://doi.org/10.1063/1.4979914
3. G. Piazza, P. Stephanou, and A. Pisano. Piezoelectric aluminum nitride vibrating contour-mode MEMS resonators. J. Microelectromech. Syst. 2006;15:1406–1418. https://doi.org/10.1109/JMEMS.2006.886012
4. M. Rinaldi, C. Zuniga, C. Zuo, and G. Piazza. Super-high-frequency two port AlN contour-mode resonators for RF applications. IEEE Trans. Ultrason. Ferroelectr. Freq. Control 2009;57:38–45. https://doi.org/10.1109/TUFFC.2010.1376
5. V. Yantchev and I. Katardjiev. Micromachined thin film plate acoustic resonators utilizing the lowest order symmetric lamb wave mode. IEEE Trans.Ultrason. Ferroelectr. Freq. Control 2006;54:87–95. https://doi.org/10.1109/TUFFC.2007.214
6. Y. Xiao, J. Han, K. Zhu, and G.Wu. A piezoelectric mechanically coupled Lamé mode resonator with ultra-high Q. Appl. Phys. Lett. 2023;122:114101. https://doi.org/10.1063/5.0141778
7. Y. Zou, C. Gao, J. Zhou, Y. Liu, Q. Xu, Y. Qu, W. Liu, J. Soon, Y. Cai, and C. Sun. Aluminum scandium nitride thin-film bulk acoustic resonators for 5G wideband applications. Microsyst. Nanoeng. 2022;8:1–7. https://doi.org/10.1038/s41378-022-00457-0
8. J. Segovia-Fernandez, M. Cremonesi, C. Cassella, A. Frangi, and G. Piazza. Anchor Losses in AlN Contour Mode Resonators. J. Microelectromech. Syst. 2015;24:265–275. https://doi.org/10.1109/JMEMS.2014.2367418
9. C. Lin, Y. Lai, J. Hsu, Y. Chen, D. Senesky, and A. Pisano. High-Q aluminum nitride Lamb wave resonators with biconvex edges. Appl. Phys. Lett. 2011;99:143501. https://doi.org/10.1063/1.3643153
10. B. Harrington and R. Abdolvand. In-plane acoustic reflectors for reducing effective anchor loss in lateral–extensional MEMS resonators. J. Micromech. Microeng. 2011;21:085021. https://doi.org/10.1088/0960-1317/21/8/085021
11. R. Abdolvand, H. Lavasani, G. Ho, and F. Ayazi. Thin-film piezoelectricon-silicon resonators for high-frequency reference oscillator applications. IEEE Trans. Ultrason. Ferroelectr. Freq. Control 2008;55:2596–2606. https://doi.org/10.1109/TUFFC.2008.976
12. G. Pillai and S.-S. Li. Quality factor boosting of bulk acoustic wave resonators based on a two dimensional array of high-Q resonant tanks. Appl. Phys. Lett. 2020;116:085021. https://doi.org/10.1063/5.0007418
13. R. Yang, Y. Zhang, J. Qian, and J.-Y. Lee. Effect of Phononic Crystal Orientation on AlN-on-Silicon Lamb Wave Micromechanical Resonators. IEEE Sens. J. 2022;22:16811–16819. https://doi.org/10.1109/JSEN.2022.3192088
14. V. Gokhale and J. Gorman. Approaching the intrinsic quality factor limit for micromechanical bulk acoustic resonators using phononic crystal tethers. Appl. Phys. Lett. 2017;111:013501. https://doi.org/10.1063/1.4990960

15. L. Binci, C. Tu, H. Zhu, and J. Lee. Planar ring-shaped phononic crystal anchoring boundaries for enhancing the quality factor of Lamb mode resonators. Appl. Phys. Lett. 2016;109:203501. https://doi.org/10.1063/1.4967794
16. H. Huang, Z. Tan, S. Huo, L. Feng, J. Chen, and X. Han. Topologically protected zero refraction of elastic waves in pseudospin-hall phononic crystals. Commun. Phys. 2020;3:46. https://doi.org/10.1038/s42005-020-0314-6
17. M. Siddiqi and J. Lee. Wide acoustic bandgap solid disk-shaped Phononic crystal anchoring boundaries for enhancing quality factor in AlN-on-Si mems resonators. Micromachines 2018;9:413. https://doi.org/10.3390/mi9080413
18. E. Coffy, S. Euphrasie, P. Vairac, and A. Khelif. Experimental evidence of high spatial confinement of elastic energy in a phononic cantilever. Appl. Phys. Lett. 2021;119:203501. https://doi.org/10.1063/5.0062930
19. J. Segovia-Fernandez and G. Piazza. Thermoelastic damping in the electrodes determines Q of AlN contour mode resonators. J. Microelectromech. Syst. 2017;26:550–558. https://doi.org/10.1109/JMEMS.2017.2672962
20. Z. Hao and B. Liao. An analytical study on interfacial dissipation in piezoelectric rectangular block resonators with in-plane longitudinal-mode vibrations. Sens. Actuator A Phys. 2010;163,:401–409.
21. Y. Wang, Y. Wang, and X. Su. Large bandgaps of two-dimensional phononic crystals with cross-like holes. J. Appl. Phys. 2011;110:113520. https://doi.org/10.1063/1.3665205
22. R. Lu, T. Manzaneque, Y. Yang, and S. Gong. Lithium Niobate Phononic Crystals for Tailoring Performance of RF Laterally Vibrating Devices. IEEE Trans. Ultrason. Ferroelectr. Freq. Control 2018;65:934. https://doi.org/10.1016/j.sna.2010.08.023
23. Y. Wang and Y. Wang. Multiple wide complete bandgaps of two dimensional phononic crystal slabs with cross-like holes. J. Sound Vib. 2013;332:2019–2037. https://doi.org/10.1016/j.jsv.2012.11.031
24. O. Bilal and M. Hussein. Ultrawide phononic band gap for combined in plane and out-of-plane waves. Phys. Rev. E 2011;84:065701. https://doi.org/10.1103/PhysRevE.84.065701
25. H.-W. Dong, X.-X. Su, Y.-S. Wang, and C. Zhang. Topological optimization of two-dimensional phononic crystals based on the finite element method and genetic algorithm. Struct Multidiscipl Optim 50, 593–604(2014). https://doi.org/10.1007/s00158-014-1070-6
26. J. Chen, J. Zhang, and S. Huo. Multi-objective optimization of asymmetric acoustic transmission with periodical structure. Ultrasonics 2018;82:252260. https://doi.org/10.1016/j.ultras.2017.09.007
27. H.-W. Dong, X.-X. Su, and Y.-S. Wang. Multi-objective optimization of two-dimensional porous phononic crystals. J. Phys. D 2014;47:155301. https://doi/org/10.1088/0022-3727/47/15/155301
28. Y. Li, X. Huang, and S. Zhou. Topological Design of Cellular Phononic Band Gap Crystals. Materials 2016;9:186. https://doi.org/10.3390/ma9030186
29. M. Kushwaha, P. Halevi, L. Dobrzynski, and B. Djafari-Rouhani. Acoustic band structure of periodic elastic composites. Phys. Rev. Lett. 1993;71:2022. https://doi.org/10.1103/PhysRevLett.71.2022
30. L. D'Alessandro, B. Bahr, L. Daniel, D. Weinstein, and R. Ardito. Shape optimization of solid–air porous phononic crystal slabs with widest full 3D bandgap for in-plane acoustic waves. J. Comput. Phys. 2017;344:465–484. https://doi.org/10.1016/j.jcp.2017.05.018
31. I. Veres and T. Berer. Complexity of band structures: Semi-analytical finite element analysis of one-dimensional surface phononic crystals. Phys. Rev. B 2012;86:104304. https://doi.org/10.1103/PhysRevB.86.104304
32. J. Wortman and R. Evans. Young's modulus, shear modulus, and Poisson's ratio in silicon and germanium. J. Appl. Phys. 1965;36:153–156. https://doi.org/10.1063/1.1713863
33. T. Wu, Z. Huang, and S. Lin. Surface and bulk acoustic waves in two-dimensional phononic crystal consisting of materials with general anisotropy. Phys. Rev. B 2004;69:094301. https://doi.org/10.1103/PhysRevB.69.094301
34. J. Jin, S. Jiang, H. H. L. Zhan, X. Wang, and V. Laude. Acousto-optic cavity coupling in 2d phoxonic crystal with combined convex and concave holes. J. Appl. Phys. 2021;130:123104. https://doi.org/10.1063/5.0060412
35. I. Pavlov, A. Vasiliev, and A. Porubov. Dispersion properties of the phononic crystal consisting of ellipse-shaped particles. J. Sound Vib. 2016;384:163–176. https://doi.org/10.1016/j.jsv.2016.08.012
36. P. Peng, J. Mei, and Y. Wu. Lumped model for rotational modes in phononic crystals. Phys. Rev. B 2012;86:134304. https://doi.org/10.1103/PhysRevB.86.134304
37. M. Hopcroft, W. Nix, and T. Kenny. What is the Young's Modulus of Silicon?. J. Microelectromech. Syst. 2010;19:229–238. https://doi.org/10.1109/JMEMS.2009.2039697
38. A. Cowen, G. Hames, K. Glukh, and B. Hardy. PiezoMUMPs design handbook, MEMSCAP Inc 1; 2014.
39. J. D. Larson, P. D. Bradley, S. Wartenberg, and R. C. Ruby. Modified Butterworth-Van Dyke circuit for FBAR resonators and automated measurement system. in 2000 IEEE IUS pp.863–868. https://doi.org/10.1109/ULTSYM.2000.922679
40. M. Kurosu, D. Hatanaka, K. Onomitsu, and H. Yamaguchi. On-chip temporal focusing of elastic waves in a phononic crystal waveguide. Nat. Commun. 2018;9:1331. https://doi.org/10.1038/s41467-018-03726-7
41. A. Khelif, A. Choujaa, S. Benchabane, B. Djafari-Rouhani, and V. Laude. Guiding and bending of acoustic waves in highly confined phononic crystal waveguides. Appl. Phys. Lett. 2004;84:4400. https://doi.org/10.1063/1.1757642

Author photo and biography

Zihao Xie received the B.S. degree from the Zhejiang University, Hangzhou, China, in 2021. He is currently pursuing the Ph.D. degree with the School of Mechanical Engineering, Zhejiang University, Hangzhou, China. His research interests include acoustic waves in piezoelectric devices and microelectromechanical system (MEMS) resonators for radio frequency microsystems.

Yongqing Fu received the Ph.D. degree from Nanyang Technological University, Singapore, in 1999. He was a Research Fellow with the Singapore–MIT Alliance, Singapore, and a Research Associate with the University of Cambridge, Cambridge, U.K. He was a Reader with the Thin Film Centre, University of West of Scotland, Glasgow, U.K., and a Lecturer with Heriot-Watt University, Edinburgh, U.K. He is currently a Professor with Northumbria University, Newcastle Upon Tyne, U.K. He has extensive experience in smart thin film/materials, biomedical microdevices, energy materials, lab-on-chip, micromechanics, MEMS, nanotechnology, sensors, and microfluidics. He has established a worldwide reputation from his pioneer research work on shape memory films, piezoelectric thin films, nanostructured composite/films for applications in MEMS, sensing, and renewable energy applications. He has authored and coauthored about 150 refereed international journal articles, one book on thin-film shape memory alloys, and ten book chapters in these areas.

Jin Xie received Ph.D. degree from Nanyang Technological University, Singapore, in 2008. From 2007–2011, he worked in Institute of Microelectronics, Singapore. In June 2011, he joined the Department of Mechanical Engineering, University of California, Berkeley, CA, USA, as a post-doc researcher. In October 2012, he joined the School of Mechanical Engineering, Zhejiang University, Hangzhou, China, as a professor. His research interests include microelectromechanical systems (MEMS) design and processes, micro sensors and actuators.